

Anisotropic spin-density distribution and magnetic anisotropy of strained thin films: Angle-dependent x-ray magnetic circular dichroism

G. Shibata,^{1,*} M. Kitamura,² M. Minohara,² K. Yoshimatsu,^{1,2} T. Kadono,¹ K. Ishigami,¹ T. Harano,¹ Y. Takahashi,¹ S. Sakamoto,¹ Y. Nonaka,¹ K. Ikeda,¹ Z. Chi,¹ M. Furuse,³ S. Fuchino,³ M. Okano,³ J.-i. Fujihira,⁴ A. Uchida,⁴ K. Watanabe,⁴ H. Fujihira,⁴ S. Fujihira,⁴ A. Tanaka,⁵ H. Kumigashira,² T. Koide,² and A. Fujimori¹

¹*Department of Physics, University of Tokyo,*

Bunkyo-ku, Tokyo 113-0033, Japan

²*Photon Factory, Institute of Materials Structure Science,*

High Energy Accelerator Research Organization (KEK), Tsukuba, Ibaraki 305-0801, Japan

³*National Institute of Advanced Industrial Science and*

Technology (AIST), Tsukuba, Ibaraki 305-8568, Japan

⁴*Fujihira Co., Ltd., Tsukuba, Ibaraki 305-0047, Japan*

⁵*Department of Quantum Matter, Graduate School of Advanced Sciences of Matter,*

Hiroshima University, Higashi-Hiroshima, Hiroshima 739-8530, Japan

(Dated: December 14, 2024)

Abstract

Magnetic anisotropies of ferromagnetic thin films are induced by epitaxial strain from the substrate via strain-induced anisotropy in the orbital magnetic moment and that in the spatial distribution of spin-polarized electrons. However, the orbital polarization of $\text{La}_{1-x}\text{Sr}_x\text{MnO}_3$ (LSMO) thin films studied by x-ray linear dichroism (XLD) has always been found out-of-plane for both tensile and compressive epitaxial strain and hence irrespective of the magnetic anisotropy. In order to resolve this mystery, we directly probed the *orbital polarization of spin-polarized electrons* by angle-dependent x-ray magnetic circular dichroism (XMCD) measurements on LSMO thin films under tensile and compressive strain. Anisotropy of the spin-density distribution was found to be in-plane for the tensile strain and out-of-plane for the compressive strain, consistent with the observed magnetic anisotropy. The ubiquitous out-of-plane orbital polarization seen by XLD is attributed to the occupation of both spin-up and spin-down out-of-plane orbitals in the surface magnetic dead layer.

Magnetic anisotropy is one of the most important properties of ferromagnets and its external control has been a major challenge both from the fundamental and applied science points of view¹. From the application point of view, enhancement of the magnetic anisotropy is necessary to realize magnets with high coercive fields, which can be utilized as high-density energy-storage magnets. From the scientific point of view, elucidating the microscopic origin of magnetic anisotropy has been an important issue because it is generally governed by the complex interplay between spin-orbit interaction and microscopic electronic states such as spin and orbital magnetic moments, band structures, and anisotropy of charge/spin densities. Especially, the magnetic anisotropy of ferromagnetic thin films is of great interest and importance because it can be controlled, e.g., by changing epitaxial strain and film thickness.

As for oxide materials, the perovskite-type manganese oxide $\text{La}_{1-x}\text{Sr}_x\text{MnO}_3$ (LSMO) has been the most extensively studied ferromagnet due to its intriguing physical properties such as colossal magnetoresistance (CMR) and half-metallicity. The physical properties of LSMO can be controlled in various ways, e.g., by changing hole concentration x , temperature T , and external magnetic field H (Ref. 2). In the case of thin films, their properties are also strongly affected by epitaxial strain which originates from the lattice mismatch between the film and the substrate. For example, Konishi *et al.*³ have shown that ferromagnetic (FM) metallic LSMO ($x = 0.3-0.5$) thin films enter the A-type antiferromagnetic (AFM) metallic phase under tensile strain from a SrTiO_3 (STO) (001) substrate and the C-type AFM insulating phase under compressive strain from a LaAlO_3 (LAO) (001) substrate. The magnetic anisotropy of the LSMO thin films also depends on the epitaxial strain: the magnetic easy axes are in-plane when grown on the STO substrate and out-of-plane when grown on the LAO substrate^{4,5}. First-principles calculations have predicted that the $d_{x^2-y^2}$ orbital is preferentially occupied under the tensile strain and that the $d_{3z^2-r^2}$ orbital is preferentially occupied under the compressive strain³. However, previous x-ray linear dichroism (XLD) experiments have shown that the $d_{3z^2-r^2}$ orbital is preferentially occupied for both STO and LAO substrates⁶⁻⁸. This apparent discrepancy with theory has been ascribed to the different orbital occupation between the surface and the bulk, that is, the spatial symmetry breaking at the surface leads to the preferential occupation of the $d_{3z^2-r^2}$ orbital⁶⁻⁸. Thus, the microscopic electronic and magnetic states of LSMO thin films and their relationship with the macroscopic magnetic properties have remained elusive so far.

In the present work, we have employed an alternative method which directly probes the

orbital occupation of spin-polarized electrons using angular-dependent x-ray magnetic circular dichroism (XMCD) in core-level x-ray absorption spectroscopy (XAS). In the XMCD spin sum rule⁹, in addition to the well-known term which represents the spin magnetic moment \mathbf{M}_{spin} , there is an additional term called ‘magnetic dipole term’ \mathbf{M}_{T} which represents the spatial anisotropy of spin-density distribution, namely, the orbital shapes of the spin-polarized electrons. While XLD is sensitive to the orbital polarization of *all* the valence electrons, XMCD is sensitive to the orbital polarization of only *spin-polarized* electrons and, therefore, one can directly probe the orbital states of electrons which contribute to the ferromagnetism. In general, it is difficult to deduce \mathbf{M}_{spin} and \mathbf{M}_{T} separately from a single XMCD spectrum. However, as we shall see below, one can separate XMCD spectra into the \mathbf{M}_{spin} and \mathbf{M}_{T} components because the angular dependencies of XMCD originating from \mathbf{M}_{spin} and \mathbf{M}_{T} are different^{10–13}. Hence, the spatial anisotropy of the spin-polarized electrons in the ferromagnetic materials can be deduced in addition to the total spin magnetic moment. Especially, in the geometry where \mathbf{M}_{spin} is perpendicular to the incident x rays [so-called transverse XMCD (TXMCD) geometry]¹¹, one can extract the pure \mathbf{M}_{T} component.

Although TXMCD was theoretically proposed two decades ago^{10–13}, there have been only few experimental reports^{14–17} because the direction of the magnetic field is fixed parallel or nearly parallel to the incident x rays in conventional XMCD measurement systems. Recently, we have developed an apparatus for angle-dependent XMCD experiments using a vector-type magnet where the direction of the magnetic field can be rotated using two pairs of superconducting magnets¹⁸. In this paper, we report on the angle-dependent XMCD and TXMCD experiments on ferromagnetic LSMO ($x = 0.3$) thin films grown on STO and LAO substrates, and investigate the effect of epitaxial strain on the orbital states of spin-polarized electrons. We have revealed that the LSMO thin film under tensile (compressive) strain has $d_{x^2-y^2}$ -like ($d_{3z^2-r^2}$ -like) spin-density distribution, which is different from the charge-density distribution deduced from the XLD measurements. The origin of the difference between the spin- and charge-density distributions is attributed to the preferential occupation of both the spin-up and spin-down $d_{3z^2-r^2}$ orbitals at the surface, which suggests the formation of magnetic dead layers at the surface.

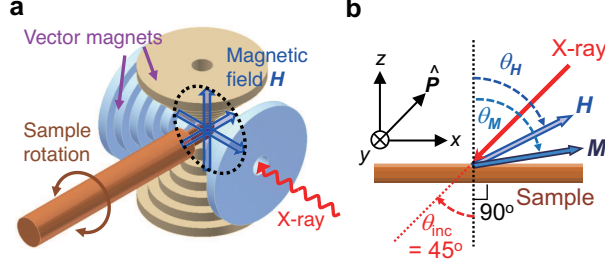


Figure 1. Experimental geometry of angle-dependent x-ray magnetic circular dichroism (XMCD). (a) Schematic drawing of the experimental setup. (b) Definition of the angles of incident x rays (θ_{inc}), magnetic field (θ_H), and magnetization (θ_M). θ_{inc} was fixed at 45° in the present work. \hat{P} is a unit vector along the x-ray incident direction, which is defined to be antiparallel to the wavevector of x rays k .

RESULTS

Angular dependence of XMCD spectra and TXMCD.

Figure 1a shows a schematic drawing of the experimental setup for angle-dependent XMCD. One can change the direction of the external magnetic field using two sets of superconducting magnets orthogonally arranged. The sample can also be rotated around the same axis. The experimental geometry is schematically drawn in Fig. 1b with the definition of the angles of incident x rays (θ_{inc}), applied magnetic field (θ_H), and magnetization (θ_M). Note that in general θ_M is not equal to θ_H unless the applied magnetic field is large enough to fully align all the electron spins along the magnetic field direction. According to XMCD sum rules^{9,19}, the XMCD intensity is proportional to $\hat{P} \cdot \mathbf{M}_{\text{spin}}$ (where \hat{P} is a unit vector along the x-ray incident direction), under the assumption that the spin magnetic moment \mathbf{M}_{spin} dominates \mathbf{M} and that the orbital magnetic moment \mathbf{M}_{orb} and the magnetic dipole moment \mathbf{M}_T are much smaller than \mathbf{M}_{spin} . (For more information about angle-dependent XMCD, see Supplementary Note 1.) In the present study, θ_{inc} was fixed to 45° and θ_M was varied through varying θ_H .

We have grown LSMO ($x = 0.3$) thin films on the Nb-doped STO (tensile strain) and LAO (compressive strain) substrates by the laser molecular beam epitaxy method (See ‘Methods’ section for the detail of sample preparation, and Supplementary Figs. 2, 3 and Supplementary Note 2 for sample characterization.) Figures 2a and 2b show the Mn $L_{2,3}$ -edge ($2p \rightarrow 3d$)

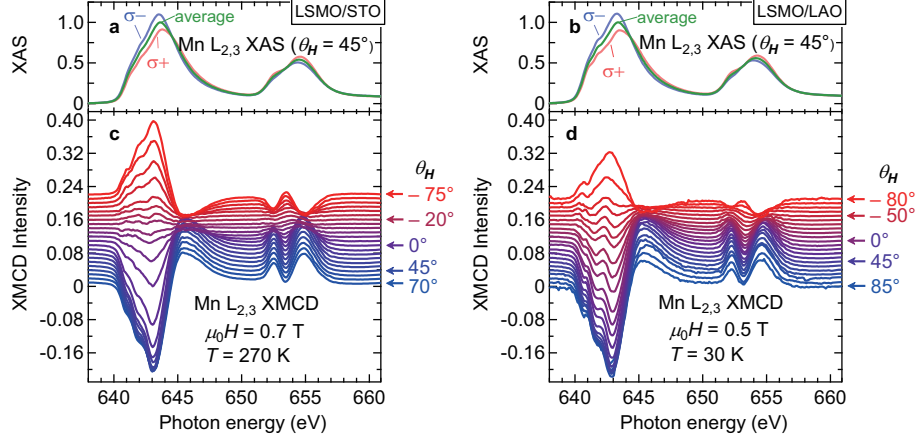


Figure 2. X-ray absorption spectroscopy (XAS) and angle-dependent XMCD at the Mn $L_{2,3}$ absorption edge. (a, b) XAS spectra of the LSMO/STO and LSMO/LAO thin films, respectively. The light red and light blue curves are the absorption spectra for the positive ($\sigma+$) and negative ($\sigma-$) helicity photons, respectively, and the green curves are the absorption spectra averaged over both the helicities. The spectra have been normalized so that the height of the averaged XAS spectra is equal to unity. (c, d) θ_H dependence of the XMCD spectra of the LSMO/STO and LSMO/LAO thin films, respectively. For the experimental geometry, see Fig. 1.

XAS spectra of the LSMO thin films grown on the STO and LAO substrates, respectively, taken at $\theta_H = 45^\circ$ (where the magnetic field is applied perpendicular to the film). Since the spectral line shape of XAS was almost independent of θ_H (see Supplementary Figure 4), only the XAS spectra for $\theta_H = 45^\circ$ are shown here. The spectral line shape of XAS is similar to those obtained in previous XMCD studies of bulk²⁰ and thin-film^{7,21} samples, and absorption signals of extrinsic Mn^{2+} (Ref. 22) are hardly observed. Figures 2c and 2d show the Mn $L_{2,3}$ -edge XMCD spectra of both the substrates for various θ_H s. Systematic changes in the XMCD intensity (proportional to $\hat{\mathbf{P}} \cdot \mathbf{M}_{\text{spin}}$) can be seen which arises from the change in the magnetization direction θ_M under varying θ_H . The XMCD spectra reverse in sign around $\theta_H \simeq -20^\circ$ for the LSMO/STO film and around $\theta_H \simeq -50^\circ$ for the LSMO/LAO film. This means that the magnetization is directed nearly perpendicular to the incident x rays ($\hat{\mathbf{P}} \cdot \mathbf{M}_{\text{spin}} \sim \hat{\mathbf{P}} \cdot \mathbf{M} \sim 0$) around these θ_H s, namely, the TXMCD geometry is realized.

The orange and green curves in Fig. 3a shows the expanded XMCD spectra at the TXMCD geometry, for the LSMO/STO and LSMO/LAO thin films, respectively. Finite TXMCD signals, which reflects the magnetic dipole term \mathbf{M}_T , are clearly observed. The

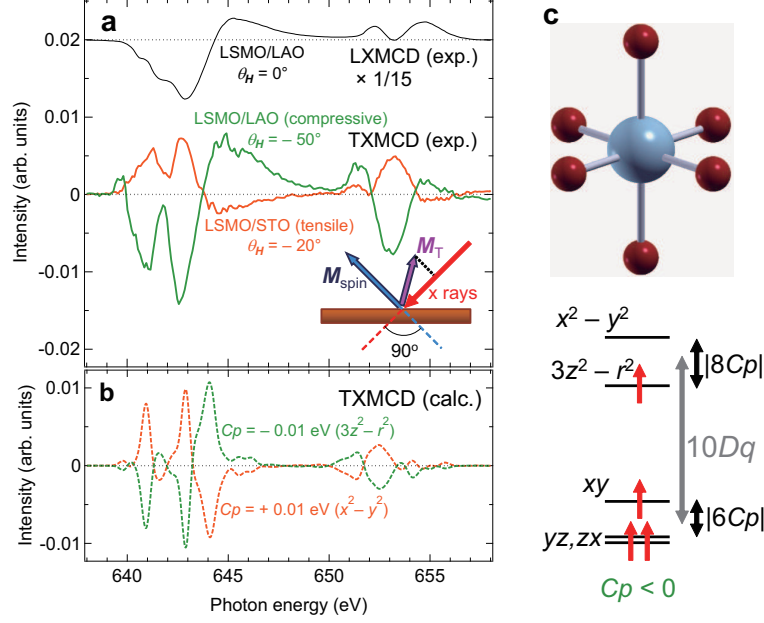


Figure 3. Transverse XMCD (TXMCD). (a) Experimental TXMCD spectra of the LSMO thin films on the STO (orange) and LAO (green) substrates compared with the longitudinal XMCD spectra (black). Inset shows the schematic drawing of the TXMCD geometry. (b) Calculated TXMCD spectra based on the Mn³⁺O₆ cluster model with D_{4h} symmetry. (c) Schematic drawing of the Mn³⁺O₆ cluster with D_{4h} symmetry and the energy levels of Mn 3d electrons. Here, C_p is a parameter proportional to the crystal-field splitting between the $x^2 - y^2$ and $3z^2 - r^2$ levels¹⁶, and $C_p = +0.01$ eV ($C_p = -0.01$ eV) corresponds to the case where the $x^2 - y^2$ ($3z^2 - r^2$) level has lower energy than the $3z^2 - r^2$ ($x^2 - y^2$) level. Panel c describes the case of $C_p < 0$. The parameter values used for the cluster-model calculation are listed in Supplementary Table 1.

spectral line shapes are quite different from those of conventional (longitudinal) XMCD (black curve in Fig. 3a), ruling out the possibility that \mathbf{M}_{spin} is not precisely perpendicular to the x rays with the result that the misaligned \mathbf{M}_{spin} produces the XMCD signals. Furthermore, the spectral line shapes of LSMO/STO and LSMO/LAO are nearly identical but only the sign of the spectra is reversed. This suggests that the sign of \mathbf{M}_T , namely the anisotropy of the spin-density distribution, is reversed reflecting the opposite epitaxial strain.

In order to further confirm that the obtained spectra arise from genuine TXMCD, we have calculated the TXMCD spectra under tensile or compressive strain using the Mn³⁺O₆ cluster model with D_{4h} symmetry (see ‘Method’ section for details). Here, only the Mn³⁺

(d^4) valence state has been considered since the anisotropy of the charge/spin density is negligible for the Mn^{4+} (d^3) valence state, where the $t_{2g\uparrow}$ levels are fully occupied and the $e_{g\uparrow}$ levels are empty. Using the parameter values listed in Supplementary Table 1, we have calculated the TXMCD spectra corresponding to both tensile and compressive strain, as shown in Fig. 3b. The calculated TXMCD spectra well reproduce the experimental ones, supporting that the experimentally obtained spectra are the genuine TXMCD signal which reflects the anisotropic spin density on the Mn atom. Comparing the sign of the experimental TXMCD spectra with the calculated ones, it is clearly demonstrated that the spin-density distribution of the Mn 3d electrons in the LSMO/STO (LSMO/LAO) thin film is more $d_{x^2-y^2}$ -like ($d_{3z^2-r^2}$ -like), consistent with the expectation for the tensile and compressive epitaxial strain from the substrates.

Quantitative estimate of magnetic anisotropy energy and anisotropic spin-density distribution.

We have seen in Figs. 2c and 2d that the sign change of $\hat{\mathbf{P}} \cdot \mathbf{M}_{\text{spin}}$ occurs around $\theta_{\mathbf{H}} \simeq -20^\circ$ for the LSMO/STO film and $\theta_{\mathbf{H}} \simeq -50^\circ$ for the LSMO/LAO film. If there were no magnetic anisotropy, $\theta_{\mathbf{M}}$ should be equal to $\theta_{\mathbf{H}}$ and the sign change should occur around $\theta_{\mathbf{H}} = -45^\circ$, where the incident x-ray beam is perpendicular to the magnetic field. The deviation of the sign change angle from $\theta_{\mathbf{H}} = -45^\circ$ in the present experiment indicates that $\theta_{\mathbf{M}}$ is not equal to $\theta_{\mathbf{H}}$ due to finite magnetic anisotropy. This offers the possibility to deduce the sign and magnitude of the magnetic anisotropy by fitting the measured angular dependence of the XMCD intensity to the theoretical one which incorporates the effect of magnetic anisotropy.

Figures 4a and 4b show the $\theta_{\mathbf{H}}$ dependence of the projected effective spin magnetic moment $\hat{\mathbf{P}} \cdot \mathbf{M}_{\text{spin}}^{\text{eff}}$ ($\equiv \hat{\mathbf{P}} \cdot [\mathbf{M}_{\text{spin}} + (7/2)\mathbf{M}_{\text{T}}] \simeq \hat{\mathbf{P}} \cdot \mathbf{M}_{\text{spin}}$) obtained by applying the sum rule⁹ to the XMCD spectra in Figs. 2c (STO substrate) and 2d (LAO substrate), respectively. The obtained angular dependencies are different from the ones which assume $\theta_{\mathbf{H}} = \theta_{\mathbf{M}}$ (black dashed curves), indicating that the effect of magnetic anisotropy has to be taken into account. We have, therefore, simulated the obtained angular dependence of $\hat{\mathbf{P}} \cdot \mathbf{M}_{\text{spin}}^{\text{eff}}$ ($\simeq \hat{\mathbf{P}} \cdot \mathbf{M}_{\text{spin}}$) based on the Stoner-Wohlfarth model²³. In this model, one assumes a single magnetic domain and that only the uniaxial component of the lowest order for the magnetic anisotropy. Then, the magnetic energy (per volume) E is given by an expression which contains $\theta_{\mathbf{M}}$

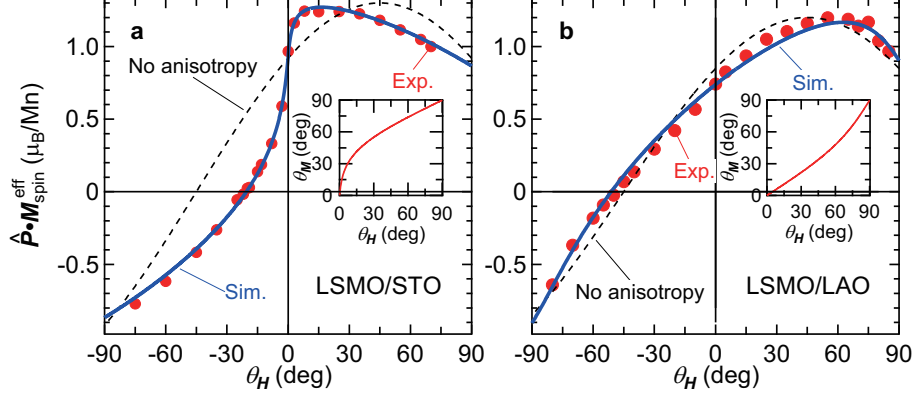


Figure 4. Angular dependence of the projected magnetic moment. (a, b) θ_H -dependencies of the projected effective spin magnetic moment $\hat{\mathbf{P}} \cdot \mathbf{M}_{\text{spin}}^{\text{eff}}$ ($\sim \hat{\mathbf{P}} \cdot \mathbf{M}_{\text{spin}}$) deduced from the experimental data using spin XMCD sum rule⁹ (circle) and its simulations. **a** and **b** are the data for the LSMO/STO and LSMO/LAO thin films, respectively. The black dashed curve describes the case where there is no magnetic anisotropy, and the blue solid curve describes the case where the shape anisotropy and magnetocrystalline anisotropy (MCA) are taken into account. Inset shows the θ_M vs θ_H relation deduced from the simulation. For the experimental geometry, see Fig. 1.

(see the ‘Method’ section for more detail). By minimizing E with respect to θ_M for each θ_H , one can deduce θ_M as a function of θ_H , and can calculate the projected magnetic moment $\hat{\mathbf{P}} \cdot \mathbf{M}_{\text{spin}}^{\text{eff}} \equiv \hat{\mathbf{P}} \cdot [\mathbf{M}_{\text{spin}} + (7/2)\mathbf{M}_T]$ using the deduced θ_M . It is also possible to deduce the uniaxial magnetocrystalline anisotropy (MCA) constant K_u , the saturation magnetization M_{sat} , and the electric quadrupole moment $\langle Q_{zz} \rangle \equiv \langle 1 - 3\hat{z}^2 \rangle$ by taking these variables as parameters and fitting the simulated angular dependence to the experimental one. The results of the simulations are shown in Figs. 4a and 4b by blue solid curves, showing good agreement with experiment. The best-fit parameter values are listed in Table I. The K_u values in Table I ($K_u > 0$ corresponding to out-of-plane easy axis) clearly show that finite MCA is present in the LSMO/STO (LSMO/LAO) thin film which favors in-plane (out-of-plane) easy magnetization, consistent with the present (Supplementary Fig. 3) and previous^{4,5} magnetic measurements. Table I also shows that the electric quadrupole moment $\langle Q_{zz} \rangle = \langle 1 - 3\hat{z}^2 \rangle$ is positive (negative) for the STO (LAO) substrate. Since $(7/2)\langle Q_{zz} \rangle = +2$ for the $d_{x^2-y^2}$ orbital and $(7/2)\langle Q_{zz} \rangle = -2$ for the $d_{3z^2-r^2}$ orbital¹⁰, the positive (negative) $\langle Q_{zz} \rangle$ for the LSMO/STO (LSMO/LAO) film implies that the charge distribution of spin-

Table I. Best-fit parameters for the simulated curves in Figs. 4a and 4b. Note that K_u represents the MCA energy excluding shape anisotropy.

Substrate	M_{sat} (μ_B/Mn)	K_u (kJ/m ³)	$(7/2)\langle Q_{zz} \rangle$
STO	1.26 ± 0.04	-38 ± 3	$+0.05 \pm 0.04$
LAO	1.20 ± 0.01	30 ± 7	-0.13 ± 0.03

polarized electrons, namely, the distribution of the spin density, is more $x^2 - y^2$ -like for the STO (tensile) substrate and more $3z^2 - r^2$ -like for the LAO (compressive) substrate. This supports the TXMCD result that the spin-density distribution in the strained LSMO thin films is anisotropic.

The advantage of the present method in deducing the magnetic anisotropy from the angle-dependent XMCD is that one can eliminate the effect of extrinsic spectral changes due to the saturation effect²⁴, because the incident angle of the x rays is fixed. In addition, this method can be used in principle for dilute magnetic systems such as ultrathin films and lightly-doped magnetic semiconductors, for which the conventional SQUID magnetometry is hardly applicable, offering the possibility of estimating the magnetic anisotropy of these systems more accurately.

DISCUSSION

The deduced anisotropic spin distribution in the LSMO thin films ($x^2 - y^2$ -like in the case of the STO substrate and $3z^2 - r^2$ -like in the case of the LAO substrate) is consistent with the orbital polarization expected from the strain from the substrate. It is also consistent with the orbital ordering which has been suggested by the transport and magnetic measurements and the density-functional calculation³. On the other hand, the results of XLD measurements⁶ show that the $d_{3z^2-r^2}$ orbital is more preferentially occupied than the $d_{x^2-y^2}$ orbital even in the case of tensile strain (STO substrate), and has been attributed to the symmetry breaking at the surface and interface⁸. The reason why the XMCD result is consistent with the transport and density-functional results, reflecting the bulk properties in spite of its surface sensitivity comparable to XLD, may become apparent if one notices that XMCD is sensitive only to the *spin-polarized* electrons while XLD is sensitive to *all* the d

electrons. If the majority part of the surface Mn atoms occupies the $d_{3z^2-r^2}$ orbital due to the symmetry-breaking effect but are not spin-polarized, the $3z^2 - r^2$ -like charge-density distribution at the surface and interface should be observed in the XLD measurements, while the $x^2 - y^2$ -like spin-density distribution from underneath layers should be observed in the XMCD measurements. Indeed, there have been several reports which suggest the presence of magnetic dead layers at the surface or the interface of the FM LSMO thin films^{25,26}. The present angle-dependent XMCD and TXMCD studies, therefore, indicate close connection between the magnetic dead layer and the $3z^2 - r^2$ -like preferential orbital occupation at the surface of LSMO thin films.

METHODS

Sample preparation.

LSMO ($x = 0.3$) thin films were grown on Nb-doped STO (001) and undoped LAO (001) (in the pseudo-cubic notation) substrates by laser molecular beam epitaxy²⁷. Since the lattice constant of bulk LSMO is smaller (larger) than that of STO (LAO), the film is under tensile (compressive) strain from the STO (LAO) substrate. The thickness of the thin films was around 100 monolayers (~ 40 nm) for both samples. The growth rate was estimated from the intensity oscillation of the specular spot in reflection high-energy electron diffraction (RHEED) during the growth. The LSMO films were deposited at the temperature of 1050 °C on the STO substrate and 650 °C on the LAO substrate, under the oxygen pressure of 1×10^{-4} Torr. After the growth of the films, both samples were annealed at 400 °C for 45 minutes under 1 atm of O₂ to fill oxygen vacancies. The out-of-plane lattice constants of the films were evaluated by synchrotron x-ray diffraction (XRD) measurements at BL-7C of Photon Factory, High Energy Accelerator Research Organization (KEK-PF). The magnetization measurements were performed using a superconducting quantum interference device (SQUID) magnetometry.

XMCD measurements.

The XAS and XMCD measurements were performed using a vector-magnet XMCD apparatus¹⁸ with circularly polarized soft x rays at the helical undulator beam line BL-16A2

of KEK-PF. The measurement temperature T for the LSMO/LAO film was 30 K, while it was set to 270 K for the LSMO/STO film. A lower T was chosen for the LSMO/LAO film because the saturation magnetization at room temperature was low³, while a higher T was chosen for the LSMO/STO film because the magnetic anisotropy at low temperature was too large to saturate the magnetization along the magnetic hard axis (out-of-plane direction). The spectra were taken in the total electron yield mode, which is a relatively surface-sensitive measurement mode (with a probing depth of $\lambda \sim 3$ nm)²⁴. The measurements were performed at a pressure of 1×10^{-9} Torr. The intensity of the incident x rays was monitored by a photocurrent from the post-focusing mirror.

Cluster-model calculation.

The cluster-model calculation was performed based on the method described in Ref. 28, using the ‘Xtls’ code (version 8.5) developed by Arata Tanaka. A distorted Mn^{3+}O_6 octahedral cluster with D_{4h} symmetry (elongated or shrunk along the [001] direction) was used. The Mn $3d$, Mn $2p$ core, and O $2p$ orbitals were taken as basis functions. Charge transfer from the ligand O $2p$ to the Mn $3d$ orbitals was taken into account, and we considered three electron configurations for both the initial and final states: $2p^6 3d^4$, $2p^6 3d^5 \underline{L}$, and $2p^6 3d^6 \underline{L}^2$ for the initial state, and $2p^5 3d^5$, $2p^5 3d^6 \underline{L}$, and $2p^5 3d^7 \underline{L}^2$ for the final state. We adjusted the following parameters to reproduce the experimental TXMCD spectra: U_{dd} (Mn $3d$ - $3d$ Coulomb energy), U_{pd} (Mn $2p$ - $3d$ Coulomb energy), Δ (charge-transfer energy), $(pd\sigma)$ (Slater-Koster parameter between Mn $3d$ and O $2p$), and $10Dq$ (crystal-field splitting between the e_g and t_{2g} levels). The magnitude of the D_{4h} crystal-field splitting $8Cp$ (splitting between the $x^2 - y^2$ and $3z^2 - r^2$ levels)¹⁶ was fixed to 0.08 eV and only its sign was varied, because varying the magnitude of $8Cp$ only changed the magnitude of XMCD and did not change the spectral line shape. We neglected the anisotropy of transfer integrals due to the D_{4h} symmetry of the MnO_6 cluster and transfer integrals between the O $2p$ orbitals, in order to reduce the number of adjustable parameters. The x-ray incident angle was chosen to be in the [101] direction, and the effect of external magnetic field was incorporated as a molecular field of 0.01 eV along the $[\bar{1}01]$ direction. The calculated spectra were broadened by a Voigt function (convolution of a Lorentzian with a half width at half maximum (HWHM) of 0.33 eV and a Gaussian with a HWHM of 0.3 eV) to obtain the XAS spectrum for each circular

polarization. The optimized parameter values are listed in Supplementary Table 1.

Simulation of angular dependence of $\hat{\mathbf{P}} \cdot \mathbf{M}_{\text{spin}}$ based on the Stoner-Wohlfarth model.

We have adopted the Stoner-Wohlfarth model²³ in order to simulate the angular dependence of the projected effective spin magnetic moment $\hat{\mathbf{P}} \cdot \mathbf{M}_{\text{spin}}^{\text{eff}}$ ($\simeq \hat{\mathbf{P}} \cdot \mathbf{M}_{\text{spin}}$) in Figs. 4a and 4b. By assuming that the film has only a single magnetic domain and that the magnetic anisotropy has only the uniaxial component of the lowest order, the magnetic energy (per volume) E can be expressed as

$$E = -\mu_0 M_{\text{sat}} H \cos(\theta_{\mathbf{M}} - \theta_{\mathbf{H}}) + \frac{\mu_0}{2} M_{\text{sat}}^2 \cos^2 \theta_{\mathbf{M}} - K_{\text{u}} \cos^2 \theta_{\mathbf{M}}, \quad (1)$$

where H is the magnitude of the external magnetic field, M_{sat} is the saturation magnetization, and K_{u} is the uniaxial anisotropy constant for MCA ($K_{\text{u}} > 0$ for out-of-plane easy axis). The three terms in Eq. 1 represent the Zeeman energy due to the applied magnetic field, the shape anisotropy which originates from the demagnetization field in the film, and the magnetocrystalline anisotropy (MCA) which originates from a combined effect of microscopic electron occupation and spin-orbit interaction. By minimizing E with respect to $\theta_{\mathbf{M}}$, we deduced $\theta_{\mathbf{M}}$ as a function of $\theta_{\mathbf{H}}$, H , K_{u} , and M_{sat} . Then, the projection of the effective spin magnetic moment $\hat{\mathbf{P}} \cdot \mathbf{M}_{\text{spin}}^{\text{eff}} \equiv \hat{\mathbf{P}} \cdot [\mathbf{M}_{\text{spin}} + (7/2)\mathbf{M}_{\text{T}}]$ was calculated using the deduced $\theta_{\mathbf{M}}$ by the following equation:

$$\begin{aligned} & \hat{\mathbf{P}} \cdot \mathbf{M}_{\text{spin}} + (7/2)\hat{\mathbf{P}} \cdot \mathbf{M}_{\text{T}} \\ &= M_{\text{sat}} \cos(\theta_{\mathbf{M}} - \theta_{\text{inc}}) + (7/4)\langle Q_{zz} \rangle M_{\text{sat}} (2 \cos \theta_{\mathbf{M}} \cos \theta_{\text{inc}} - \sin \theta_{\mathbf{M}} \sin \theta_{\text{inc}}), \end{aligned} \quad (2)$$

where $\langle Q_{zz} \rangle \equiv \langle 1 - 3\hat{z}^2 \rangle$ is the electric quadrupole moment [For the derivation of Eq. (2), see Supplementary Note 1]. This gives the $\theta_{\mathbf{H}}$ dependence of the projected moment $\hat{\mathbf{P}} \cdot \mathbf{M}_{\text{spin}}^{\text{eff}}$ for a set of parameters (K_{u} , M_{sat} , and $\langle Q_{zz} \rangle$). The obtained $\theta_{\mathbf{H}}$ dependence was fitted to the experimental one (Fig. 4a,b) to deduce K_{u} , M_{sat} , and $\langle Q_{zz} \rangle$ using the least-square method.

ACKNOWLEDGMENTS

We would like to thank Kenta Amemiya, Masako Sakamaki, and Reiji Kumai for valuable technical support at KEK-PF. We would also like to thank Hiroki Wadati for providing us

with information about the XLD studies of LSMO thin films. This work was supported by a Grant-in-Aid for Scientific Research from the JSPS (22224005, 15H02109, 15K17696). The experiment was done under the approval of the Photon Factory Program Advisory Committee (proposal No. 2016S2-005, No. 2013S2-004, No. 2016G066, No. 2014G177, No. 2012G667, and 2015S2-005). Part of this work was performed using a SQUID magnetometer at the Cryogenic Research Center, the University of Tokyo. G.S. acknowledges support from Advanced Leading Graduate Course for Photon Science (ALPS) at the University of Tokyo and the JSPS Research Fellowships for Young Scientists (Project No. 26.11615). A.F. is an adjunct member of Center for Spintronics Research Network (CSRN), the University of Tokyo, under Spintronics Research Network of Japan (Spin-RNJ).

AUTHOR CONTRIBUTIONS

G.S., K.Y., T.Kadono, K.Ishigami, T.H., Y.T, S.S., Y.N., K.Ikeda, and Z.C. performed XMCD measurements with the assistance of T.Koide and A.F. M.K., M.M., and K.Y. grew and characterized thin films with the assistance of H.K. M.F., M.O., S.Fuchino, A.U., and J.-i.F. developed the vector-type superconducting magnet. J.-i.F., A.U., K.W., H.F., K.Ishigami, T.H., Y.N., T.Kadono, Y.T., S.S., K.Ikeda, Z.C., and G.S. were involved in the design, construction, and improvement of the XMCD measurement chamber, with assistance of S.Fujihira, T.Koide, and A.F. G.S. analyzed the XMCD data and performed the cluster-model calculation. A.T. developed the code for the cluster-model calculation (Xtls version 8.5). G.S. and A.F. wrote the manuscript with suggestions by M.K., M.M., K.Y., T.Koide, and all the other coauthors. A.F. was responsible for overall project direction and planning.

COMPETING FINANCIAL INTERESTS:

The authors declare no competing financial interests.

* email: shibata@wyvern.phys.s.u-tokyo.ac.jp

¹ Coey, J. M. D. *Magnetism and Magnetic Materials* (Cambridge University Press, New York, 2009).

- ² Imada, M., Fujimori, A. & Tokura, Y. Metal-insulator transitions. *Rev. Mod. Phys.* **70**, 1039–1263 (1998).
- ³ Konishi, Y. *et al.* Orbital-state-mediated phase-control of manganites. *J. Phys. Soc. Jpn.* **68**, 3790–3793 (1999).
- ⁴ Tsui, F., Smoak, M. C., Nath, T. K. & Eom, C. B. Strain-dependent magnetic phase diagram of epitaxial $\text{La}_{0.67}\text{Sr}_{0.33}\text{MnO}_3$ thin films. *Appl. Phys. Lett.* **76**, 2421–2423 (2000).
- ⁵ Kwon, C. *et al.* Stress-induced effects in epitaxial $(\text{La}_{0.7}\text{Sr}_{0.3})\text{MnO}_3$ films. *J. Magn. Magn. Mater.* **172**, 229 – 236 (1997).
- ⁶ Tebano, A. *et al.* Evidence of orbital reconstruction at interfaces in ultrathin $\text{La}_{0.67}\text{Sr}_{0.33}\text{MnO}_3$ films. *Phys. Rev. Lett.* **100**, 137401 (2008).
- ⁷ Aruta, C. *et al.* Orbital occupation, atomic moments, and magnetic ordering at interfaces of manganite thin films. *Phys. Rev. B* **80**, 014431 (2009).
- ⁸ Pesquera, D. *et al.* Surface symmetry-breaking and strain effects on orbital occupancy in transition metal perovskite epitaxial films. *Nat. Commun.* **3**, 1189 (2012).
- ⁹ Carra, P., Thole, B. T., Altarelli, M. & Wang, X. X-ray circular dichroism and local magnetic fields. *Phys. Rev. Lett.* **70**, 694–697 (1993).
- ¹⁰ Stöhr, J. & König, H. Determination of spin- and orbital-moment anisotropies in transition metals by angle-dependent x-ray magnetic circular dichroism. *Phys. Rev. Lett.* **75**, 3748–3751 (1995).
- ¹¹ Dürr, H. A. & van der Laan, G. Magnetic circular x-ray dichroism in transverse geometry: Importance of noncollinear ground state moments. *Phys. Rev. B* **54**, R760–R763 (1996).
- ¹² van der Laan, G. Microscopic origin of magnetocrystalline anisotropy in transition metal thin films. *J. Phys. Condens. Matter* **10**, 3239 (1998).
- ¹³ van der Laan, G. Relation between the angular dependence of magnetic x-ray dichroism and anisotropic ground-state moments. *Phys. Rev. B* **57**, 5250–5258 (1998).
- ¹⁴ Dürr, H. A. *et al.* Element-specific magnetic anisotropy determined by transverse magnetic circular x-ray dichroism. *Science* **277**, 213–215 (1997).
- ¹⁵ Mamiya, K. *et al.* Angle-resolved soft X-ray magnetic circular dichroism in a monatomic Fe layer facing an $\text{MgO}(0\ 0\ 1)$ tunnel barrier. *Radiat. Phys. Chem.* **75**, 1872–1877 (2006).
- ¹⁶ van der Laan, G., Chopdekar, R. V., Suzuki, Y. & Arenholz, E. Strain-induced changes in the electronic structure of MnCr_2O_4 thin films probed by x-ray magnetic circular dichroism. *Phys.*

- Rev. Lett.* **105**, 067405 (2010).
- ¹⁷ Koide, T. *et al.* Gigantic transverse x-ray magnetic circular dichroism in ultrathin Co in Au/Co/Au(001). *J. Phys. Conf. Ser.* **502**, 012002 (2014).
 - ¹⁸ Furuse, M. *et al.* HTS vector magnet for magnetic circular dichroism measurement. *IEEE Trans. Appl. Supercond.* **23**, 4100704 (2013).
 - ¹⁹ Thole, B. T., Carra, P., Sette, F. & van der Laan, G. X-ray circular dichroism as a probe of orbital magnetization. *Phys. Rev. Lett.* **68**, 1943–1946 (1992).
 - ²⁰ Koide, T. *et al.* Close correlation between the magnetic moments, lattice distortions, and hybridization in LaMnO₃ and La_{1-x}Sr_xMnO_{3+δ}: Doping-dependent magnetic circular x-ray dichroism study. *Phys. Rev. Lett.* **87**, 246404 (2001).
 - ²¹ Shibata, G. *et al.* Thickness-dependent ferromagnetic metal to paramagnetic insulator transition in La_{0.6}Sr_{0.4}MnO₃ thin films studied by x-ray magnetic circular dichroism. *Phys. Rev. B* **89**, 235123 (2014).
 - ²² de Jong, M. P. *et al.* Evidence for Mn²⁺ ions at surfaces of La_{0.7}Sr_{0.3}MnO₃ thin films. *Phys. Rev. B* **71**, 014434 (2005).
 - ²³ Stoner, E. C. & Wohlfarth, E. P. A mechanism of magnetic hysteresis in heterogeneous alloys. *Philos. Trans. R. Soc. London, Ser. A* **240**, 599–642 (1948).
 - ²⁴ Nakajima, R., Stöhr, J. & Idzerda, Y. U. Electron-yield saturation effects in *L*-edge x-ray magnetic circular dichroism spectra of Fe, Co, and Ni. *Phys. Rev. B* **59**, 6421–6429 (1999).
 - ²⁵ Yoshimatsu, K., Horiba, K., Kumigashira, H., Ikenaga, E. & Oshima, M. Thickness dependent electronic structure of La_{0.6}Sr_{0.4}MnO₃ layer in SrTiO₃/La_{0.6}Sr_{0.4}MnO₃/SrTiO₃ heterostructures studied by hard x-ray photoemission spectroscopy. *Appl. Phys. Lett.* **94**, 071901–1–3 (2009).
 - ²⁶ Huijben, M. *et al.* Critical thickness and orbital ordering in ultrathin La_{0.7}Sr_{0.3}MnO₃ films. *Phys. Rev. B* **78**, 094413 (2008).
 - ²⁷ Horiba, K. *et al.* A high-resolution synchrotron-radiation angle-resolved photoemission spectrometer with *in situ* oxide thin film growth capability. *Rev. Sci. Instrum.* **74**, 3406–3412 (2003).
 - ²⁸ Tanaka, A. & Jo, T. Resonant 3*d*, 3*p* and 3*s* photoemission in transition metal oxides predicted at 2*p* threshold. *J. Phys. Soc. Jpn.* **63**, 2788–2807 (1994).